

RESEARCH ARTICLE

10.1002/2016JC011737

Special Section:

Physical Processes
Responsible for Material
Transport in the Gulf of
Mexico for Oil Spill
Applications

Key Points:

- The structure of buoyant plumes in stratified environments is strongly affected by rotation
- Radial cyclostrophic balance generates an adverse vertical pressure gradient
- Even moderate system rotation organizes an anticyclonic precession of the plume axis

Supporting Information:

- Supporting Information S1
- Movie S1
- Movie S2
- Movie S3

Correspondence to:

A. Fabregat Tomàs,
alex.fabregat@csi.cuny.edu

Citation:

Fabregat Tomàs, A., A. C. Poje, T. M. Özgökmen, and W. K. Dewar (2016), Effects of rotation on turbulent buoyant plumes in stratified environments, *J. Geophys. Res. Oceans*, 121, 5397–5417, doi:10.1002/2016JC011737.

Received 22 FEB 2016

Accepted 13 JUN 2016

Accepted article online 16 JUN 2016

Published online 5 AUG 2016

Effects of rotation on turbulent buoyant plumes in stratified environments

Alexandre Fabregat Tomàs¹, Andrew C. Poje¹, Tamay M. Özgökmen², and William K. Dewar³

¹Department of Mathematics, City University of New York, New York, New York, USA, ²Rosenstiel School of Marine and Atmospheric Science, University of Miami, Miami, Florida, USA, ³Earth, Ocean and Atmospheric Science, Florida State University, Tallahassee, Florida, USA

Abstract We numerically investigate the effects of rotation on the turbulent dynamics of thermally driven buoyant plumes in stratified environments at the large Rossby numbers characteristic of deep oceanic releases. When compared to nonrotating environments, rotating plumes are distinguished by a significant decrease in vertical buoyancy and momentum fluxes leading to lower and thicker neutrally buoyant intrusion layers. The primary dynamic effect of background rotation is the concentration of entraining fluid into a strong cyclonic flow at the base of the plume resulting in cyclogeostrophic balance in the radial momentum equation. The structure of this cyclogeostrophic balance moving upward from the well head is associated with a net adverse vertical pressure gradient producing an inverted hydrostatic balance in the mean vertical momentum budgets. The present simulations reveal that the primary response to the adverse pressure gradient is an off-axis deflection of the plume that evolves into a robust, organized anticyclonic radial precession about the buoyancy source. The off-axis evolution is responsible for the weaker inertial overshoots, the increased thickness of lateral intrusion layers, and the overall decrease in the vertical extent of rotating plumes at intermediate Rossby numbers compared to the nonrotating case. For inlet buoyancy forcings and environmental Rossby numbers consistent with those expected in deepwater blowout plumes, the speed of the organized precession is found to be as large as typical oceanic cross-flow speeds.

1. Introduction

On 20 April 2010, an explosion occurred on the Deep Water Horizon drilling rig, located in the Gulf of Mexico, killing 11 people and injuring 17 others [Graham *et al.*, 2011]. This was the beginning of the Deep Water Horizon (DwH) oil spill, an event that lasted for 87 days. The spill went through several phases: the initial phase where the deep pipe leaked from two locations, the phase where the pipe was cut, localizing the spill to the well head and last, additions of various collecting structures. In addition, dispersants were supplied at the well head [Plume Calculation Team, 2010]. The spill was large (4.9 million barrels of oil and about 5.3 million barrels of gas) [Lehr *et al.*, 2010] and considerable effort went into oil recovery, burning of surface oil and clean up of beaches dirtied by oil. Not all of the DwH oil surfaced. Precise numbers are hard to come by, but something like 15–30% of the oil remained subsurface [Lubchenko *et al.*, 2012; McNutt *et al.*, 2012]. Knowledge of how and where in the water column the plume fluid detrains is important for assessing subsurface oil ecosystem impacts.

Although verified scaling laws for plume metrics exist for many plume types, the deep ocean oil spill problem presents a host of new modeling challenges. The inlet buoyancy fluxes, produced by a multiphase mixture of oil and gas at elevated temperatures, are extremely large. The background flow is highly irregular on a broad range of space and time scales, and the environment hosts ecosystems and chemistry that interact with and are strongly affected by the effluent. Given the duration and location of the DwH event, rotation and stratification are likely to play important roles.

The purpose of this paper is to isolate the combined effects of rotation (characterized by the rotation frequency f) and stratification (characterized by the buoyancy frequency N) on plume dynamics in order to understand and quantify how rotation, at representative values of the Rossby number $Ro = N/f$, may modify overall transport in the initial stages of the plume. To this end, we consider the simplest possible setting,

namely the Boussinesq behavior of a single phase, thermal plume evolving in a quiescent, thermally stratified environment with constant density gradient. Despite these severe simplifications, such plumes retain much of the essential physics governing a deepwater release, namely a narrow near field core that entrains ambient fluid, an intrusion, or spreading level where the input buoyancy anomaly has been erased by turbulent entrainment and an inertial overshoot region above the intrusion level. What is lacking in the single phase approach is the presence of multiple intrusion levels driven by the slip velocity of secondary phases relative to that of the ambient water [Socolofsky and Adams, 2005; Fabregat et al., 2015].

Due to their importance in both industrial and geophysical settings, plumes evolving in either stratified or rotating environments have been the subject of considerable research. Large-Eddy Simulations (LES) have been used to investigate the symmetry breaking due to rotation on plumes in cross-flows [Lavelle, 1997]. The dynamics of tilted plumes in unstratified environments was studied by Sheremet [2004] and ensemble statistics of individual plumes in rotating Rayleigh-Bénard convection were discussed in Julien et al. [1999]. Plumes created by rotating sources in uniform environments were studied by Pham et al. [2011] who also conducted LES to analyze the dependence of the vertical development of turbulent thermal plumes on the source rotation frequency [Pham et al., 2006]. Experiments on rotating plumes in uniform environments have also been carried out by Maxworthy and Narimousa [1994]; Fernando et al. [1998]; Goodman et al. [2004] and more recently numerical simulations of the evolution of rotating laminar plumes in small, enclosed cavities with emphasis on the stability of both axisymmetric and three-dimensional solutions were shown by Marqués and López [2014]. Rotational effects on fully turbulent, isolated, buoyant plumes in quiescent stable stratification are, however, less well detailed.

In order to understand long-term dynamics of rotating stratified plumes, Helfrich and Battisti [1991] conducted a series of experiments by injecting dense water into a salinity stratified rotating tank. Flow visualization was conducted at Rossby numbers ~ 5 and 1.5 and compared to a nonrotating case. The results indicated significant rotational effects, even at $Ro = 5$. As the Rossby number decreases from infinity, visualizations showed a thickening lateral intrusion layer “encroaching” vertically on the plume source while the extent of the inertial overshoot region above the intrusion layer is significantly reduced. The dye observations also confirmed what would be expected from geostrophic considerations, namely, the existence of two clearly differentiated regions in the flow: a cyclonic circulation near the source where the plume entrains fresh fluid as it grows in the vertical and an anticyclonic region in the lateral intrusion where the neutrally buoyant fluid spreads radially. While not explicitly discussed, experimental images clearly show rotating plumes bending off the vertical axis. In terms of the long term evolution (times greater than ~ 100 rotation periods), the authors observed two regimes. For $Ro < Ro_c \approx 2.5$, the experiments revealed the development of a mode 2 azimuthal instability eventually leading to the formation of propagating dipoles. For $Ro > Ro_c$, the plume evolves into a single baroclinic vortex that moves away from the source once the centers of the cyclonic and anticyclonic regions misalign as in a *heton* configuration.

Motivated by deep ocean thermal vents, Speer and Marshall [1995] studied the effects of rotation on the convection produced by a sustained localized buoyancy source at Rossby numbers similar to those of Helfrich and Battisti. Numerical experiments, conducted at modest resolution with Laplacian eddy-diffusivity closures, confirmed the importance of the opposite signed circulation regions and showed that the primary effect of rotation is the creation, as a consequence of angular momentum conservation, of a horizontal “stratification” that directly inhibits vertical plume growth. Consistent with experimental observations of a critical Rossby number, the numerical results indicated significant reduction in the penetration heights of rotating plumes compared to classical results for $Ro \geq 2$. For larger rotation rates, horizontal confinement leads to observed penetration heights larger than those empirically given for nonrotating plumes. The numerical model also confirmed derived scaling laws for the growth in the thickness of the anticyclonic intrusion with rotation rate.

The primary goal of the present work is to revisit these experimental, theoretical, and numerical results in the context of turbulence resolving simulations. This approach provides both direct access to time-dependent velocity and density fields and the ability to investigate fully turbulent momentum and energy budgets. Motivated by deepwater blowout plumes, we also seek to investigate rotation effects at Rossby numbers consistent with the DwH incident. Given the computational expense, we concentrate on the near field region of the plume for times less than ~ 20 rotation periods.

The paper is organized as follows. The governing equations and details of the numerical experiments are presented in section 2. Examination of instantaneous quantities is presented in section 3 with special emphasis on the plume at $Ro = 10$, a representative value of an oceanic deep water oil release. The existence of a robust, organized precession of the plume about the vertical axis in the rotating case is also discussed here. Rotation effects on integral fluxes and mean fields are discussed in sections 4 and 5. Dynamical consequences of imposed rotation are presented in terms of mean heat, momenta, and turbulent kinetic energy budgets in section 6. A summary of the results is presented in section 7.

2. Model and Numerics

2.1. Governing Equations

With the goal of quantifying the effects of system rotation on the turbulent dynamics of buoyant plumes, we consider the simplest configuration: a thermally driven, Boussinesq plume evolving in a motionless, stratified temperature environment under constant rotation. The continuity and momentum equations are

$$\nabla \cdot \tilde{\mathbf{u}} = 0 \tag{1}$$

$$\rho_r \frac{D\tilde{\mathbf{u}}}{Dt} = -\nabla \tilde{p} + \nabla \cdot \tilde{\boldsymbol{\tau}} + \rho \tilde{\mathbf{g}} - 2\tilde{\boldsymbol{\Omega}} \times \tilde{\mathbf{u}} \tag{2}$$

where ρ is the density of the fluid (with a reference value ρ_r), \tilde{p} is the pressure, $\nabla \cdot \tilde{\boldsymbol{\tau}}$ represents the viscous and turbulent stresses, $\tilde{\mathbf{g}} = (0, 0, -g)$ is the gravity acceleration vector, and $\tilde{\boldsymbol{\Omega}} = (0, 0, \omega)$ is the rotation vector and $\tilde{\cdot}$ denotes dimensional variables.

Assuming a linear equation of state for the fluid,

$$\rho = \rho_r (1 - \gamma(\tilde{T} - \tilde{T}_r)), \tag{3}$$

with a thermal expansion coefficient for the water phase $\gamma = 2 \cdot 10^{-4} \text{ K}^{-1}$ and a reference state temperature \tilde{T}_r , the system is closed with an additional conservation equation for the temperature \tilde{T} :

$$\frac{\partial \tilde{T}}{\partial \tilde{t}} + \nabla \cdot (\tilde{T} \tilde{\mathbf{u}}) = \mathcal{D}_0 \nabla^2 \tilde{T}. \tag{4}$$

In keeping with experimental practice where a passive tracer is injected at the plume source for visualization, we also consider the conservation equation for scalar concentration β ,

$$\frac{\partial \beta}{\partial \tilde{t}} + \nabla \cdot (\beta \tilde{\mathbf{u}}) = \mathcal{D}_\beta \nabla^2 \beta. \tag{5}$$

For a background environment thermally stratified with a constant slope ζ , the temperature can be decomposed into $\tilde{T}(\tilde{\mathbf{x}}, \tilde{t}) = \tilde{\theta}(\tilde{\mathbf{x}}, \tilde{t}) + \tilde{T}_r + \zeta \tilde{z}$ where $\tilde{\theta}(\tilde{\mathbf{x}}, \tilde{t})$ is the disturbance with respect to the unperturbed environment with temperature and density profiles $\tilde{T}_e(\tilde{z}) = \tilde{T}_r + \zeta \tilde{z}$ and $\rho_e = \rho_r (1 - \gamma(\tilde{T}_e - \tilde{T}_r)) = \rho_r (1 - \gamma \zeta \tilde{z})$, respectively. The associated buoyancy frequency N is then

$$N^2 = -\frac{g}{\rho_r} \frac{d\rho_e}{d\tilde{z}} = g\zeta\gamma. \tag{6}$$

With the inlet buoyancy flux B_0 defined as

$$B_0 = \tilde{g}'_0 \tilde{Q}_0 = g \tilde{Q}_0 \frac{(\rho_e^- - \rho)}{\rho_r} \Big|_{z=0} = g \tilde{A} \tilde{w}_0 \gamma \tilde{T}_0, \tag{7}$$

the transport equations (1–5) are nondimensionalized using the usual plume scaling [Socolofsky and Adams, 2005] for velocity $U_0 = (B_0 N)^{1/4}$, length $L_0 = (B_0 / N^3)^{1/4}$, time $t_0 = 1/N$, pressure $p_0 = \rho_r U_0^2$, and temperature $T_0 = \zeta L_0 \equiv (B_0 N^5)^{1/4} / (g\gamma) = 1 / (\gamma Ri)$ where Ri is the Richardson number defined below. Here \tilde{Q}_0 is the inlet volume flux, \tilde{g}'_0 is the reduced gravity at the inlet, $\tilde{A} = \pi \tilde{D}_0^2 / 4$ is the cross-section area of a circular source of diameter \tilde{D}_0 , and \tilde{w}_0 and $\tilde{T}_0 \equiv \tilde{\theta}_0$ are the inlet liquid phase velocity and temperature, respectively. Analogously, β_0 stands for the inlet passive scalar volume fraction.

The final nondimensional system of partial differential equations reads:

$$\nabla \cdot \mathbf{u} = 0 \quad (8)$$

$$\frac{D\mathbf{u}}{Dt} = -\nabla p + \frac{1}{Re} \nabla^2 \mathbf{u} + Ri \theta \hat{\mathbf{k}} - \frac{1}{Ro} \hat{\mathbf{k}} \times \mathbf{u} \quad (9)$$

$$\frac{D\theta}{Dt} = \frac{1}{Pe_T} \nabla^2 \theta - \mathbf{u} \cdot \hat{\mathbf{k}} \quad (10)$$

$$\frac{D\beta}{Dt} = \frac{1}{Pe_o} \nabla^2 \beta \quad (11)$$

where the nondimensional groups are the Reynolds number $Re = \frac{U_0 L_0}{\nu} = \frac{\sqrt{B_0 N}}{N\nu}$, the Péclet number for a scalar m $Pe_m = \frac{U_0 L_0}{D_m} = \frac{\sqrt{B_0 N}}{ND_m}$, the Rossby number $Ro = \frac{U_0}{fL_0} = \frac{N}{f}$ where f is the system rotation frequency and the Richardson number $Ri = g \frac{L_0}{U_0^2} = \frac{g}{B_0^{1/4} N^{5/4}}$. As shown in Fabregat et al. [2015], for Re of order 1000, the molecular contributions to diffusive transport are negligible and the kinematic viscosity and diffusivity for each scalar m are set at $\nu = D_m = 10^{-6} \text{ m}^2 \text{ s}^{-1}$ (Prandtl and Schmidt number for m set to one).

2.2. Numerical Experiments

The transport equations (8–11) are solved using spectral element methods (SEM) with the nek5000 [Fischer et al., 2008] package. This code has demonstrated an excellent scalability on parallel architectures and has been validated for a wide range of turbulent flow configurations. The limitations of the classic fully spectral methods in terms of geometric flexibility are overcome in SEM which allows for high-order solutions on complex grids [Deville et al., 2002]. Instead of defining a subgrid-scale (SGS) model to account for unresolved turbulent scales [Özögkmen et al., 2009a, 2009b], the numerical solution is filtered at near-grid scales using an approach similar to the Spectral Vanishing Viscosity technique [Karamanos and Karniadakis, 2000; Fischer and Mullen, 2001]. This is analogous to increasing the nominal Reynolds and Péclet numbers only at the finest scales. In all simulations, a 5% polynomial filtering of the two highest modes in the Legendre expansion has been used for every field. This approach ensures stability and preserves the exponential convergence of the solver while reducing the computational costs of computing the SGS terms. Fully developed channel simulations have shown that this procedure results in excellent agreement with Direct Numerical Simulations (DNS), it is relatively insensitive to the filter specifics and computationally efficient [Kozal et al., 2012].

In order to isolate the effects of rotation on plume dynamics, the basic flow parameters $B_0 = 5 \cdot 10^{-6} \text{ m}^4 \text{ s}^{-3}$, $N = 0.1 \text{ s}^{-1}$, $Ri \approx 3700$, $Re = Pe_m \approx 7100$, $D_0 = 0.3$, and $w_0 = 1.5$ are held constant in all experiments and f (s^{-1}) = (0, 2.5 · 10⁻³, 10⁻², 0.1) is varied. In the laboratory setting, this configuration is equivalent to a tank of $\tilde{H} = 2.6$ m height with source diameter of $\tilde{D}_0 = 8$ cm and a total temperature difference in the unperturbed background of 13.3 K. Using the inlet momentum flux $M_0 = (\pi/4) \tilde{D}_0^2 \tilde{w}_0^2$, the Morton length scale is found to be $\tilde{L}_M / L_0 = M_0^{3/4} B_0^{-1/2} / L_0 \approx 0.25$ [Shabbir and George, 1994] resulting in a jet-to-plume transition height located relatively close to the source. A weak volume forcing [Pham et al., 2007; Plourde et al., 2008; Devenish et al., 2010b] is used to accelerate the transition to turbulence in the very near field. Specifically, a 5% amplitude noise was added to the vertical velocity over a cylinder with radius $D_0/2$ and height $H/40$.

Here we concentrate on the earlier stages of plume development and for Rossby number $Ro = N/f = 10$, a representative oceanographic value, integrations are conducted for $\tilde{t}f < 20$. While considerably shorter than the expected time for the development of baroclinic instability [Helfrich and Battisti, 1991], results indicate that this time is long enough to achieve statistically stationary values of buoyancy and passive tracer concentration in the open computational domain. For comparison, Speer and Marshall find steady values for observed penetration heights and swirl velocities for $\tilde{t}f \geq 40$ for $Ro = 5$ and indications that this time decreases with decreasing rotation rate.

The nominal computational domain is a cylinder of diameter $D = 2R = \tilde{D}/L_0 = 10$ and height $H = \tilde{H}/L_0 = 10$. The domain is spatially discretized using 14th-order Legendre polynomials on 7540 elements resulting in ~22 million degrees of freedom. A detail of the SEM mesh is shown in the lower horizontal slice in Figure 1a. Experiments on buoyant plumes in stratified environments are usually limited by the accumulation of scalars in the tank. Using open (outflow) lateral boundary conditions for the momentum, the numerical simulations permit the establishment of statistically developed flow conditions and mimic the conditions of an environmental release. The far field conditions are implemented via Dirichlet zero for the scalars (θ and β).

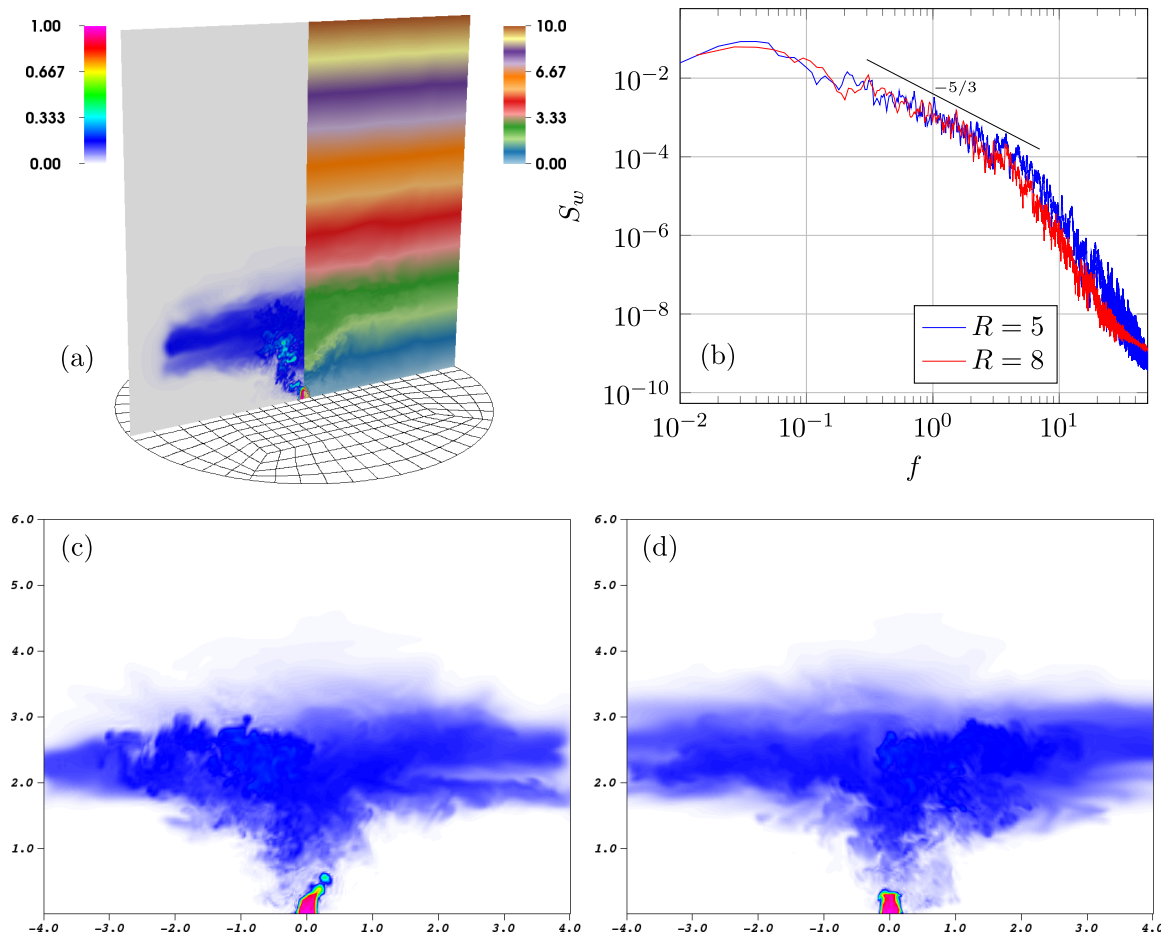


Figure 1. (top left) Vertical slices of instantaneous passive scalar volume fraction β (left half) and temperature T (right half). The horizontal slice shows the spectral element mesh. (top right) Off-axis ($r = 0.5, z = 2.5$) vertical velocity power spectrum for the thermal plumes at $Ro = 10$ with two different numerical domain sizes $R = 5$ and 8 . (bottom) Instantaneous β snapshots for $R = 5$ (left) and $R = 8$ (right).

Numerical stability at these open boundaries are ensured using numerical *sponge* regions [Applequist and Schlatter, 2014] in the radial direction where the local diffusivity coefficients for momentum and scalars smoothly increase to damp arriving perturbations. The top boundary condition is no-shear for the momentum and zero derivative for the scalars. At the bottom, Dirichlet momentum and scalars boundary conditions are used to set-up the plume source. Figure 1a shows vertical slices of the instantaneous passive scalar volume fraction β (left) and temperature T (right).

The effect of the lateral boundary conditions was analyzed by comparing results at $Ro = 10$ for two numerical domain radial sizes, $R = 5$ and $R = 8$. The resolution of the interior, nearly Cartesian, grid patch is identical in the two cases. Figures 1c and 1d show instantaneous snapshots of the passive tracer field over $r < 4$ for both $R = 5$ and $R = 8$ simulations. The vertical location and width of the lateral intrusion is unchanged indicating that the computed plume dynamics are relatively insensitive to the precise location of the lateral boundary conditions. The vertical velocity spectra at $(r, z) = (0.5, 2.5)$ shown in Figure 1b for both domains are also very similar in terms of both the low-frequency peak magnitude and the extent of the $k^{-5/3}$ inertial range.

3. Instantaneous Fields: Organized Precession

Figure 2 shows instantaneous volume plots of the passive scalar concentration β (left) and the temperature perturbation θ (right) for plumes at $Ro = \infty, 40$, and 10 taken under statistically steady conditions in the numerical domain and at $Ro = 1$ at similar integration times. The color values are identical for all Rossby numbers.

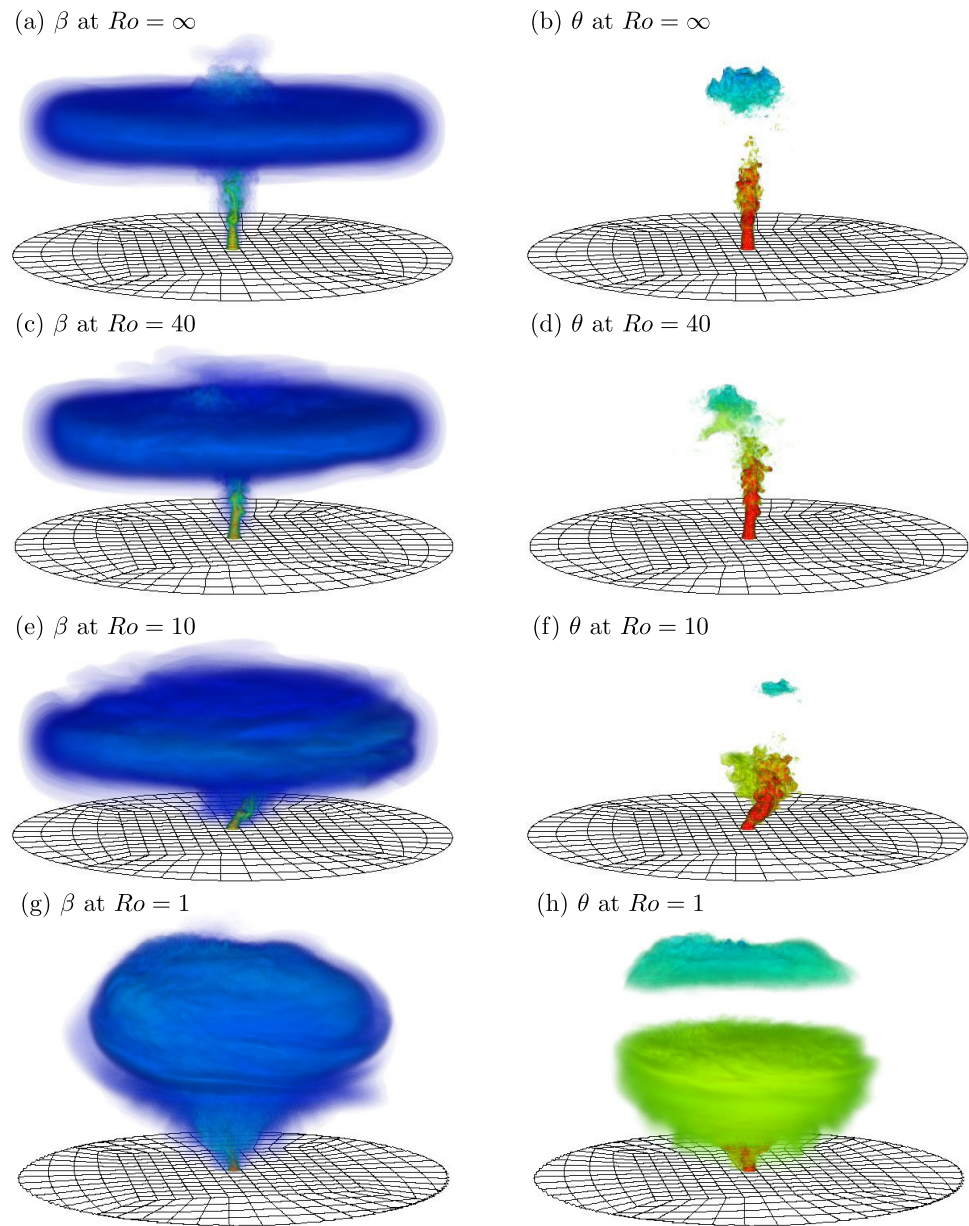


Figure 2. Volume rendering of the instantaneous passive scalar volume fraction, β , (left plots) and temperature perturbation, θ , (right plots) at various Rossby numbers. Transparency ranges from zero to one linearly over the range of β . In θ , red denotes positively buoyant and blue negatively buoyant. Gaps in perturbation temperature occur at the neutrally buoyant level where θ vanishes.

The passive scalar fields are clearly consistent with the experimental results by *Helfrich and Battisti* [1991] showing that as the rotation rate increases from $Ro = \infty$ to $Ro = 10$ (i) the lateral intrusion “encroaches” vertically on the source obscuring the plume core, (ii) the thickness of the intrusion layer increases, and (iii) the inertial overshoot region is no longer vertically aligned above the source and its extent is significantly reduced. All these rotation effects lead to an overall increase in the dispersion of the passive scalar in the vertical. Although the rotation effects on the instantaneous β field in the weakest rotation rate case at $Ro = 40$ shown in Figure 2c are very modest, the results at $Ro = 10$ shown in Figure 2e are qualitatively very similar to the experimental visualizations reported by *Helfrich and Battisti* at $Ro = 5$ [see *Helfrich and Battisti*, 1991, Figure 1]. Both clearly indicate off-axis vertical evolution of the plume fluid below the entrainment layer.

This bending of the rotating plume is more easily observed in the right plots of Figure 2 showing instantaneous temperature perturbation fields. In contrast to the nonrotating case in Figure 2b where the positively

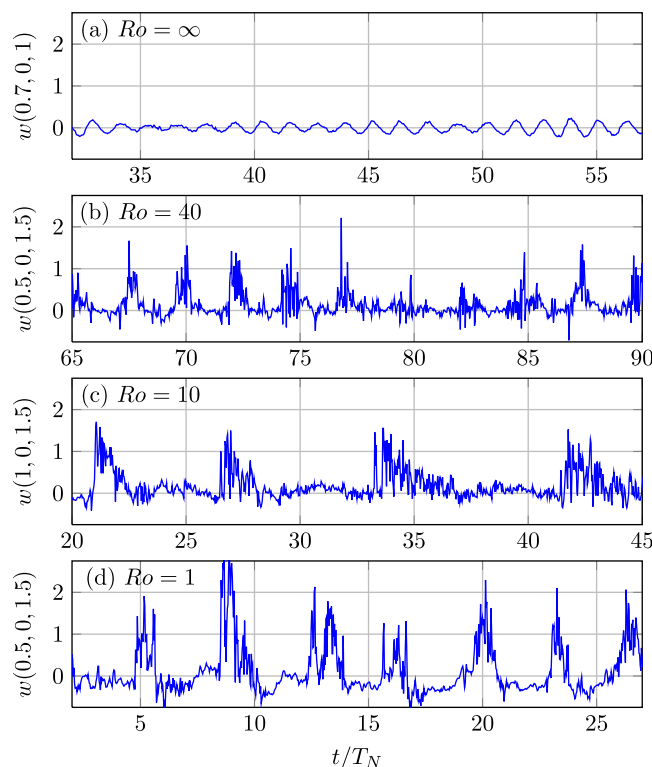


Figure 3. (top to bottom) Sample of the temporal evolution of the vertical velocity w at Rossby numbers $Ro = \infty, 40, 10,$ and 1 . The time period $\Delta t/T_N = 25$ for each Rossby number is representative of statistically developed conditions and the spatial coordinates are chosen so that the precession signal strength is maximized.

comparison to the other cases as shown in Figures 2g and 2h, respectively. While the lateral intrusion in the higher Rossby number cases eventually reaches the lateral boundaries, the plume at $Ro = 1$, with a smaller Rossby deformation radius, is confined in the numerical domain.

This change in the rotating plume dynamics between $Ro = 10$ and $Ro = 1$ is in agreement with the Helfrich and Battisti results who suggested that there is a change of regime at $Ro \approx 2.5$. For $Ro = 0.67$ and $\tilde{t}f = t/Ro \geq 225$, they observed the formation of anticyclonic-cyclonic pairs (dipoles) at the intrusion level which eventually travel away from the source. For $Ro > 3.11$ and $t/Ro \geq 108$, the plume does not break but propagates away from the source as a single baroclinic vortex. Similarly, the numerical results by Speer and Marshall [1995] suggested that for $Ro \leq 2$ horizontal confinement lead to penetration heights larger than those empirically obtained for nonrotation plumes. Although a Rossby number $\mathcal{O}(1)$ is far outside the range that any deepwater oil blowout event will ever achieve, we keep the results for this case for the sake of discussion on the Rossby number dependence of the plume dynamics.

Two animations (supporting information movies S1 and S2) show that rotating plumes are not only deflected away from the vertical, but that this deflection is eventually organized into a robust, anticyclonic azimuthal precession of the buoyant core. To demonstrate this organized precession, time traces of the vertical velocity taken at selected positions are shown in Figure 3. The signal clearly indicates the cyclical, nearly periodic appearance of the plume as a peak in w in the rotating plumes at $Ro = 40, 10,$ and 1 (Figures 3b–3d). The spatial location in each case was determined such that the strength of the precession signature is maximized.

In contrast, the axially aligned nonrotating plume in Figure 3a shows nominal fluctuating values of w at all times (time has been scaled using the nondimensional buoyancy period $T_N = 2\pi$ for clarity). The precession frequency at $(r, z) = (1, 1.5)$ in the rotating case at $Ro = 10$ in Figure 3c is estimated to be $\tilde{f}_p \approx 0.15N = 1.5f$. While the radial location of peak w is z -dependent, time traces indicate that the frequency is not.

buoyant plume (red-yellow) is aligned with the vertical axis, in the rotating cases the positive buoyancy region is deflected off-axis and mixes more vigorously at the lateral intrusion. Also, the rotation considerably reduces the extent and strength of the negatively buoyant overshoots (cyan-blue). The instantaneous θ field offer a better picture of the differences in the intensity of the plume bending between the $Ro = 40$ shown in Figure 2d and the $Ro = 10$ plume in Figure 2f. The results indicate that while at the slowest rotation the plume deflection of the axis stem is limited, the top part of the plume core exhibits a clearer off-axis location of the downdrafts.

Interestingly, the trend observed from $Ro = \infty$ to $Ro = 10$ consisting in the progressive reduction of the trapping height, changes for $Ro = 1$. With a less pronounced deflection of the plume axis in comparison to $Ro = 10$ and with a stronger inhibition of the lateral spreading due to the faster rotation rate, this plume exhibits the largest vertical extent and the faster accumulation of the scalars β and θ in compar-

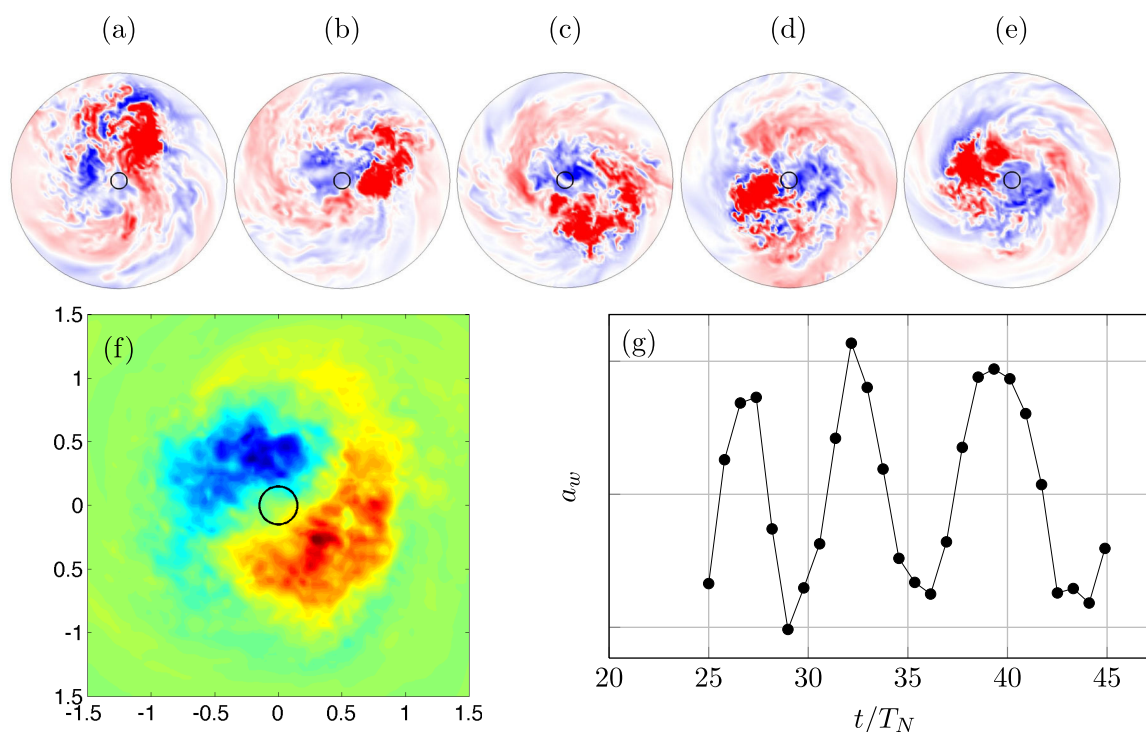


Figure 4. (a)–(e) Snapshots of the vertical velocity at t_0 , $t_0 + 1.5$, $t_0 + 3.1$, $t_0 + 4.7$, and $t_0 + 6.1$, with red positive (vertically upwards) and blue negative. (f) First eigenfunction in the Empirical Orthogonal Function analysis for w at $z = 1.5$. Red positive, blue negative, (g) Time evolution of the coefficient for the first EOF mode.

Further quantification of the periodic precession of the rotating plume can be obtained from standard Empirical Orthogonal Functions (EOF) analysis of the vertical velocity field. The principal modes for the case at $Ro = 10$ were obtained at $z = 1.5$, slightly below the intrusion layer, from 25 instantaneous snapshots collected over $\Delta t_{EOF} \approx 125$. This time span corresponds to approximately 3.2 of the precession periods observed in Figure 3. Five of these instantaneous w fields are shown in Figures 4a–4e. Positive and negative instantaneous values of vertical velocity are colored in red and blue, respectively. The sequence of images show the anticyclonic trajectory described by the plume core (dark red) around the source (black circle) during approximately one precession period.

The first of the two principal eigenfunctions explaining $\sim 50\%$ of the total variance is shown in Figure 4f. The results indicate that the dominant structure is described by a mode one azimuthal function associated with the plume-wake pair precessing around the z axis. For reference, the black circle indicates the plume source. As shown in Figure 4g, the time evolution of the coefficient of the first mode is in very good agreement with the f_p value estimated from Figure 3c. This mode one configuration is similar to that found in stability analysis of vortices in stratified environments [Riedinger *et al.*, 2010] and the stability analysis of laminar plumes in enclosed cavities [Marqués and López, 2014].

Analysis of even longer time traces indicates the persistence, and continued near-periodicity, of the organized precession. The presence of this mode, absent in the $Ro = \infty$ case, implies that rotating plumes generate a mean phase-averaged flow field that significantly alters their dynamics. In this sense, rotating stratified plumes share some of the properties observed in stratified nonrotating plumes in cross flows [Lavelle, 1997; Devenish *et al.*, 2010a] where the unidirectional current leaves gravity waves in the plume wake. In the rotating case, the periodic precession of the axis produces a plume that continually interacts with its own wake.

The observed changes in the overall shape of plumes induced by rotation can be explained by the existence of the organized precession. Instead of a single inertial overshoot aligned with the source, the precessing plume generates a ring of weaker overshoots. The associated downdrafts now periodically entrain fluid from the intrusion level toward the core, explaining the “encroaching” and eventual “obscuring” of the dyed plume observed experimentally [Helfrich and Battisti, 1991]. Although the presence of an organized

precession was not explicitly mentioned by *Helfrich and Battisti* [1991], the strong agreement between numerical and experimental snapshots of plume shape suggests that there is precession in both cases. The numerical plumes generated by *Speer and Marshall* [1995] do not show precession, or any significant breaking of axisymmetry. The simulations, however, employ relatively large effective diffusivities that may overdamp the time-dependent mode.

4. Integral Quantities

The presence of a robust, anticyclonic precession strongly affects the turbulent mixing and overall dispersion in plumes under rotation. In this section, we quantify these effects on mean volume, area, and time quantities. Mean and turbulent fields are obtained by taking temporal averages once statistically stationary conditions are reached in the open computational domain. Under periodic azimuthal precession, time-averaged fields are axisymmetric, and statistical sampling is increased here by additional averaging in the azimuthal direction.

In polar coordinates, the directional velocities are $u_r(r, \phi, z, t) = \cos(\phi)u(x, y, z, t) + \sin(\phi)v(x, y, z, t)$, $u_\phi(r, \phi, z, t) = \cos(\phi)v(x, y, z, t) - \sin(\phi)u(x, y, z, t)$ and the average of any quantity, ψ , is given by

$$\langle \psi \rangle(r, z) = \frac{1}{2\pi\Delta t} \int_0^{2\pi} \int_0^{\Delta t} \psi(r, \phi, z, \tau) d\tau d\phi. \quad (12)$$

Instantaneous variables can then be decomposed into average and fluctuating components by $\psi(r, \phi, z, t) = \langle \psi \rangle(r, z) + \psi'(r, \phi, z, t)$.

The temporal evolution of the volume integral over the computational domain of the passive scalar concentration and temperature perturbation can be used to assess the effect of rotation on overall transport and determine the time to establish statistically stationary conditions. The results for $Ro = \infty, 40, 10$, and 1 , shown in Figure 5, indicate that as the Rossby number decreases the accumulation rate of temperature perturbation (left plot) starts to diverge earlier with respect to the nonrotating case. The time taken to depart from the $Ro = \infty$ case is roughly equal to the Rossby number, i.e., it takes one system rotation period to start showing significant departures from the nonrotating case. The instantaneous total amount of θ in the domain depends on the balance between the influx at the source and the volume integral of the vertical velocity that accounts for the vertical stratification effect. The transport of θ through the lateral boundaries is a negligible contribution to the balance due to the neutral buoyancy conditions in the lateral intrusion. The development of an anticyclonic plume axis precession in the rotating case deflects the plume and leads to a reduction in the volume-averaged vertical velocity during the transient state that results in an increase of the volume integral of θ with respect to the nonrotating case. The pronounced deflection at $Ro = 10$ in comparison to the $Ro = 40$ plume explain the very limited effect in the latter. As a result, the volume

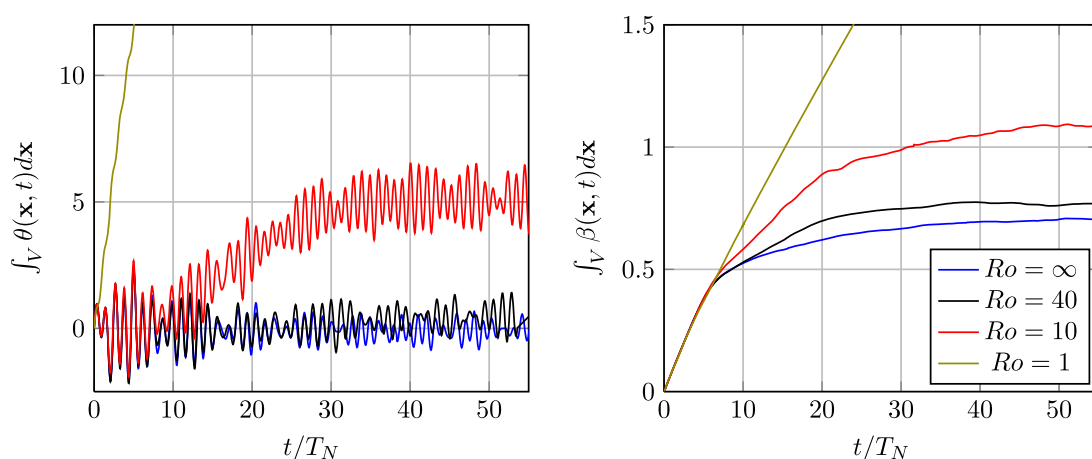


Figure 5. (left) Volume integral of θ at Rossby numbers $Ro = \infty, 40, 10$, and 1 . (right) Volume integral of β .

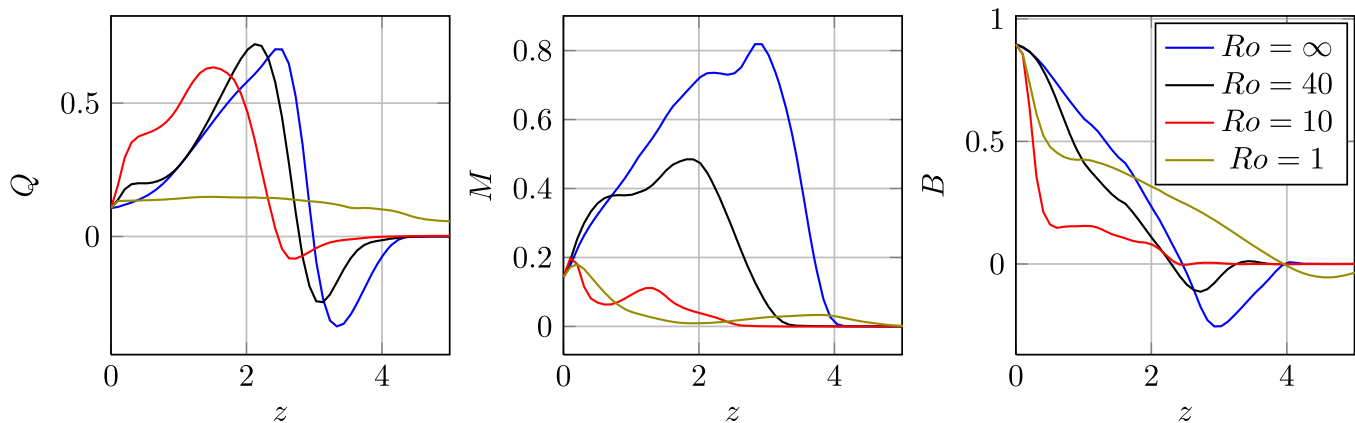


Figure 6. (left) Vertical volume Q_z for Rossby numbers $Ro = \infty, 40$ and 10 . (middle) Momentum flux M . (right) Buoyancy flux B .

integral of θ under statistically steady conditions increases as the Rossby number decreases. This can be observed in the instantaneous fields in the right plots of Figure 2 that show a reduction in the extent and strength of the negatively buoyant regions associated with the inertial overshoots.

The evolution in the volume integral of β (Figure 5, right) reaches a plateau when the source influx is balanced by the radial advective outflux through the lateral boundaries. The faster growth of the total amount of β as Ro decreases indicates that rotation reinforces the lateral confinement of the plume. This decrease in the rate at which β leaves the domain results in the thickening of the lateral intrusion as shown in the instantaneous fields in the left plots of Figure 2. The $Ro = 1$ plume, totally confined in the numerical domain, exhibits a linear growth of the volume integral of β with a slope equal to the inlet flux of this scalar. In this case, the rotation leads to a pronounced suppression of the radial entrainment in the plume and a continuous increase in the penetration height in time [Speer and Marshall, 1995].

It is important to note that while the initial time for the temporal averaging in the $Ro = \infty, 40$, and 10 cases correspond to the time when the metrics in Figure 5 reach a plateau, for the $Ro = 1$ case, such conditions never occur given the continuous growth of the confined plume. However, in order to analyze the plume dynamics dependence on the Rossby number, averages for this case were also obtained starting at a time similar to that used in the $Ro = 10$ case.

The vertical volume Q , momentum M , and buoyancy B fluxes, defined as

$$Q(z) = 2\pi \int_0^{\infty} r \langle w \rangle (r, z) dr \quad (13)$$

$$M(z) = 2\pi \int_0^{\infty} r \langle w \rangle^2 (r, z) dr \quad (14)$$

$$B(z) = 2\pi \int_0^{\infty} r \langle w \rangle (r, z) \langle g \rangle (r, z) dr, \quad (15)$$

are shown in Figure 6 for $Ro = \infty, 40, 10$, and 1 .

In agreement with the instantaneous fields of β in Figure 2, the results for the vertical evolution of the volume flux at $Ro = \infty, 40$, and 10 show that the location where the lateral intrusion starts to form, estimated from the peak in Q , decreases as the rotation rate increases. The mean rate of entrainment in the vertical, determined by integrating the continuity equation in the radial direction, can be written as $dQ/dz = -\langle r \langle u \rangle \rangle_{\infty}$. The results show that, except for the region $z \leq 0.5$ where rotation generates a modest increase in dQ/dz , the local entrainment up to the lateral intrusion location decreases as the Rossby number increases from $Ro = \infty$ to $Ro = 10$. This inhibition of the radial flux continues at the trapping height where the reversed (detrainment) flow decreases with Ro . The net entrainment, $Q_H - Q_0 = \int_0^H \frac{dQ}{dz} dz$, is very similar for the plumes at $Ro = \infty, 40$, and 10 suggesting that for these cases rotation leads to a very moderate confinement of the plume. In contrast, in the $Ro = 1$ plume the net vertical flux is dramatically reduced indicating a shut off of the net entrainment flux.

The deflection of the plume axis under rotation leads to the generation of a large radial velocity component that significantly enhances radial transport to the detriment of the vertical component. At $Ro = 40$, this deflection is very modest and barely modifies the plume alignment with respect to the z axis in the source vicinity (see Figure 2d). However, at $Ro = 10$, the deflection is very clear and the plume bending is evident at much closer locations to the source (see Figure 2f). This dramatically changes the vertical evolution of the momentum flux M as shown in the middle plot in Figure 6. As the rotation rate increases, the ability of the plume to increase the vertical transport of momentum decreases and the maximum value of M for $Ro = 10$ and $Ro = 1$ occurs at the inlet. In terms of the buoyancy flux (right plot), as Rossby number decreases from $Ro = \infty$ to $Ro = 10$ B also decreases due to the increase in the deflection angle of the plume core and enhanced lateral mixing. At $Ro = 1$, this trend reverses. Mixing within the radially confined plume destratifies the environment leading to significantly lower vertical velocities and slower decay of the buoyancy flux.

In the nonrotating case and in the context of integral solution as derived by Morton *et al.* [1956], it is possible to estimate the mean entrainment coefficient $\alpha_e = (dQ_z/dz)/(2\pi\sqrt{M})$ over the region $0 < z < 1.5$ where the stratification effects are relatively unimportant and the mean vertical velocity and temperature are assumed Gaussian. The value of $\alpha_e = 0.15$ is in excellent agreement with the numerical results for hydrothermal plumes by Jiang and Breier [2014].

5. Mean Fields

More detailed information on the differences between rotating and nonrotating cases are obtained by comparing the average passive scalar field, Figures 7a–7d, and the streamlines (colored by the mean swirl velocity), Figures 7e–7h, at $Ro = \infty$, 40, 10, and 1. For the $Ro = 10$ case, an animation showing the structure of the plume dominated by the cyclone around the plume stem and the anticyclonic circulation in the lateral intrusion is available online (supporting information movie S3).

The $\langle\beta\rangle$ results at $Ro = \infty$ shown in Figure 7a correspond to the well-known topology of nonrotating plumes in linearly stratified environments [Morton *et al.*, 1956]. The characteristic heights $z_{eq} = 2.6$ and $z_{max} = 4.2$, defined as the location where the axial mean reduced density and vertical velocity vanish, are in agreement with previous works [Devenish *et al.*, 2010b; Richards *et al.*, 2014].

The effects of increasing the rotation rate from $Ro = \infty$ to $Ro = 10$ on the lateral intrusion include an increase in the width and a reduction in its vertical location. Additionally, the vertical extent of inertial overshoots prevalent in the nonrotating plume in Figure 7a are significantly reduced as the Rossby number decreases. These effects are in agreement to the experimental observations described by Helfrich and Battisti [1991].

As discussed in section 3, these changes are intimately related to the establishment of a persistent, anticyclonic precession of the plume axis in the rotating cases. Topologically, the signature of this precession on the mean field of β consists of a plume axis deflection with respect to the vertical z axis. The relatively small deflection of the $Ro = 40$ plume in Figure 7b axis in the near-source region leads to very modest differences with respect to the nonrotating case (see also Figures 2a, 2d). However, further in the vertical, both cases exhibit clear differences and the plume top in the $Ro = 40$ case is characterized by weaker inertial overshoots and significantly smoother gradients at the trapping height location.

At $Ro = 10$, the signature of rotation on the $\langle\beta\rangle$ field is evident along the entire vertical extent of the plume as shown in Figure 7c. The mean passive scalar results are used to estimate the precession angle and the reduction in the trapping height location to be $\sim 66^\circ$ and $\sim 17\%$ with respect to the nonrotating case. The 17% reduction in the location of the trapping height is in general agreement with Speer and Marshall's observations of a 20% reduction in penetration height for $Ro = 4$ and 5.

As discussed in terms of mean vertical flux in the previous section, Figure 7d shows that the plume at $Ro = 1$ is characterized by a net entrainment shut off that confines the plume in the radial leading to a larger vertical extent and smoother scalar gradients in the plume core. In addition, the results show that the bending angle due to the precession is smaller than that at $Ro = 10$.

The streamlines at $Ro = \infty$ in Figure 7e show the flow pattern in a nonrotating plume. Below the intrusion, the fluid parcels in the plume surroundings travel horizontally as they are entrained into the plume. In the

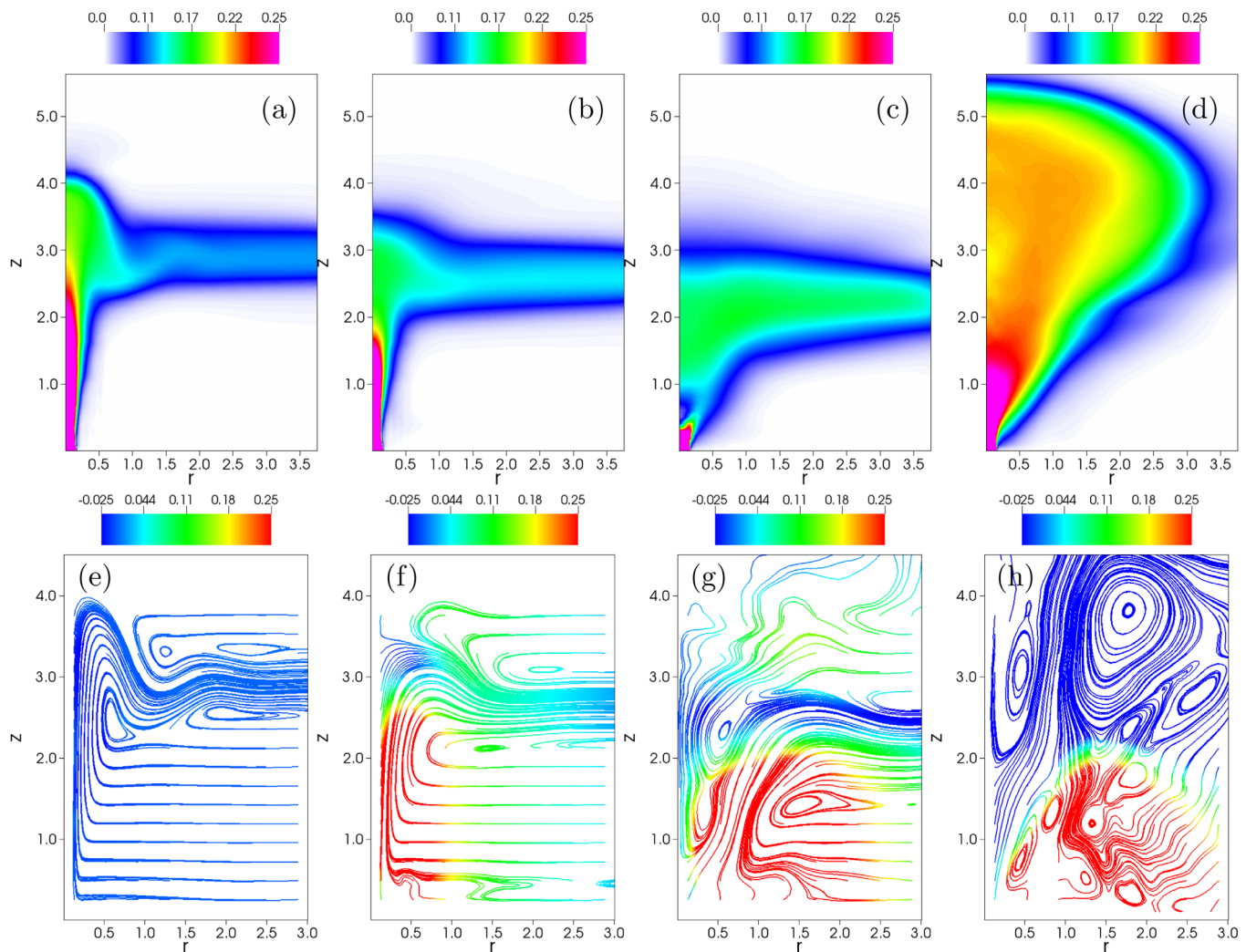


Figure 7. (left to right) Temporal and azimuthal averages of passive scalar volume fraction (top) and streamlines colored by the swirl velocity (bottom) at Rossby numbers $Ro = \infty, 40, 10,$ and $1,$ respectively.

source vicinity where the stratification effects are small, the plume width $b(z)$ is characterized by a linear growth, $b(z) \sim z$. Further in the vertical, the buoyancy flux eventually vanishes and the plume core continues to grow due to inertial effects. After reaching the maximum plume height, the negatively buoyant fluid starts falling down generating an outer ring of downdrafts around the plume top. After generating a weak undershoot due to their inertia, the fluid parcels in the downdraft spread radially at their neutral buoyancy level generating the lateral intrusion. As expected in the absence of rotation, the mean swirl velocity is virtually zero.

Once under rotation, even for the slowest rotation at $Ro = 40$, the plume exhibits a strong cyclonic circulation in the source vicinity. At $Ro = 40$, the rotation is not fast enough to noticeably deflect the plume stem. However, at the plume top, the rotation effects are apparent: the plume axis is bent, the vertical extent of the plume is reduced and the inertial overshoots and downdraft outer ring are weaker (see also Figures 2b and 2d). Notably, the streamlines also show a blockage of the entraining fluid in the bottom region associated with the establishment of a cyclostrophic balance in the radial momentum budget (see section 6.2). As suggested by the results for Q in Figure 6, this blockage in the $Ro = 40$ plume has a limited effect on the overall net entrainment.

The results at $Ro = 10$ indicate more pronounced rotational effects on the plume mean circulation. The streamlines show a marked plume axis deflection above the inlet, a decrease in the trapping height location and the appearance of recirculations between the plume and the z axes. The strengthening of the

entrainment blockage in the bottom region is accompanied by an increase in size of the cyclonic circulation and an increase in magnitude of the anticyclonic velocity in the lateral intrusion. These changes, however, do not alter significantly the net overall entrainment flux which exhibits similar values to those found at $Ro = \infty$ and $Ro = 40$ as shown in the results for Q . At $Ro = 1$, the plume mean circulation changes drastically. The streamlines show a clear suppression of the net radial entrainment into the plume that explains the much smaller values of mean vertical volume flux shown in Figure 6. In addition, the plume region is dominated by a collection of recirculation cells that explain the intense mixing in the scalar fields also observed in Figures 2g and 2h).

6. Dynamic Balances

Having shown the existence of a mean anticyclonic precession of the plume axis and discussed its effects on the turbulent mixing in rotating plumes, here we explain the mechanism that generates this distinctive feature by analyzing the budgets of heat and vertical and radial momentum at $z = 1.4$ for the Rossby numbers $Ro = \infty, 40, 10$, and 1 .

6.1. Heat

Contributions to the mean heat budget,

$$\langle u \rangle \frac{\partial \langle \theta \rangle}{\partial r} + \langle w \rangle \frac{\partial \langle \theta \rangle}{\partial z} = - \langle w \rangle - \left[\frac{1}{r} \frac{\partial \langle r \langle u' \theta' \rangle \rangle}{\partial r} + \frac{\partial \langle w' \theta' \rangle}{\partial z} \right], \quad (16)$$

are shown in Figure 8 where the thin dashed black line indicates the residual error in the balance.

Using the “thin turbulence” concept, plumes and other basic shear flows have been studied in classical turbulence texts [Tennekes and Lumley, 1972]. Specifically, for a nonrotating plume in a uniform environment, the heat balance in equation (16) reduces to

$$\langle w \rangle \frac{\partial \langle \theta \rangle}{\partial z} \approx - \frac{1}{r} \frac{\partial \langle r \langle u' \theta' \rangle \rangle}{\partial r}, \quad (17)$$

i.e., the mean vertical advective transport of heat is balanced by the radial turbulent transport. The results for the nonrotating plume ($Ro = \infty$) in a stratified environment are very similar to the balance in equation (17) given the relatively small contribution due to the mean stratification at $z = 1.4$ which is mostly balanced by the other minor contribution, the vertical turbulent transport. Although this picture of the heat budget is similar at $Ro = 40$, the two main terms in equation (17), that dominated the balance in the nonrotating case, decreased in magnitude leading to nonnegligible contributions from the stratification and the vertical heat turbulent flux.

A more dramatic change happens at $Ro = 10$. Characterized by the pronounced axis deflection of the plume, the mean vertical advective heat transport in this case is negligible. The resulting heat budget is now dominated by the turbulence transport terms and the stratification which are two orders of magnitude smaller than the main contributions in the $Ro = \infty$ case. The effects of the off-axis location of the plume core are reflected in the off-axis peaks in the radial distribution of the turbulent transport and stratification.

As shown in Figures 7a–7d, the descending intrusion layer trend observed from $Ro = \infty$ to $Ro = 10$ is broken at $Ro = 1$ that also exhibits a less pronounced plume axis deflection when compared to $Ro = 10$. This change of regime from $Ro = 10$ to $Ro = 1$ is also observed in the heat budget. The balance at $Ro = 1$, similar to that at $Ro = 40$, exhibits a significant contribution due the mean vertical advective heat transport although the magnitude is one order of magnitude smaller.

6.2. Radial Momentum

Contributions to the mean radial momentum budget,

$$\langle u \rangle \frac{\partial \langle u \rangle}{\partial r} + \langle w \rangle \frac{\partial \langle u \rangle}{\partial z} = - \frac{\partial \langle p \rangle}{\partial r} - \frac{\partial \langle u^2 \rangle}{\partial r} - \frac{\partial \langle u' w' \rangle}{\partial z} + \frac{\langle v^2 \rangle - \langle u^2 \rangle}{r} + \underbrace{\frac{\langle v \rangle^2}{CS}}_r + \underbrace{\frac{\langle v \rangle}{Ro}}_{GS}, \quad (18)$$

are shown in Figure 9. “CS” and “GS” denote “cyclotropic” and “geostrophic” terms, respectively

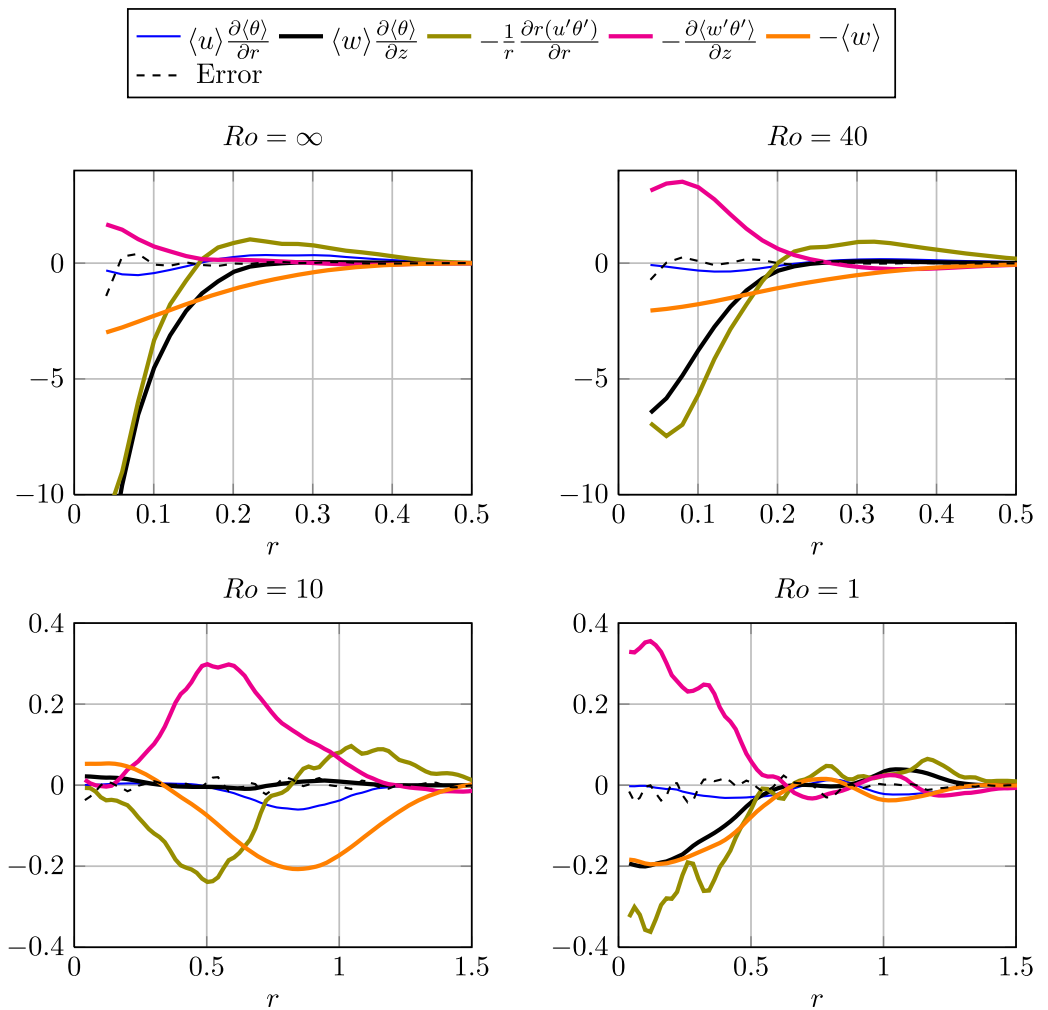


Figure 8. Heat budget at $z = 1.4$ for $Ro = \infty, 40, 10,$ and 1 .

In a nonrotating plume where the mean azimuthal velocity is zero, isotropy in the radial and azimuthal directions implies vanishing differences between $\langle u'^2 \rangle$ and $\langle v'^2 \rangle$. The turbulent radial transport balances the mean radial pressure gradient [Shabbir and George, 1994]. The radial momentum budget for the $Ro = \infty$ plume (Figure 9) confirms this balance.

Even under slow rotation, $Ro = 40$, the presence of mean azimuthal velocities modifies the classic balance with cyclostrophic terms contributing at first-order (Figure 9). The horizontal pressure gradient is now given by

$$\frac{\partial \langle p \rangle}{\partial r} \approx -\frac{\partial \langle u'^2 \rangle}{\partial r} + \frac{\langle v \rangle^2}{r}. \tag{19}$$

Although small compared to the main contributions, modest rotation also weakens isotropy in the lateral resulting in a net contribution from the turbulence terms $\langle v'^2 \rangle - \langle u'^2 \rangle$.

As the rotation rate increases to $Ro = 10$, cyclostrophy dominates the pressure balance. The overall magnitude of the radial pressure gradient and the cyclostrophic term are reduced by one order of magnitude in comparison to $Ro = \infty$. Off-axis deflection of the plume produces significant vertical turbulent transport which nearly balances radial turbulent transport. With the radial and vertical turbulent transport terms in approximate balance, equation (18) reduces to cyclostrophy, $\frac{\partial \langle p \rangle}{\partial r} \approx \frac{\langle v \rangle^2}{r}$. At even larger rotation rates, $Ro = 1$, geostrophic contributions become important and the radial pressure gradient is found to be in cyclogeostrophic balance. Compared to the $Ro = \infty$ case where the mean radial pressure gradient is totally balanced by the turbulent radial transport term, at $Ro = 1$ turbulent transport terms make negligible contributions to the radial momentum budget.

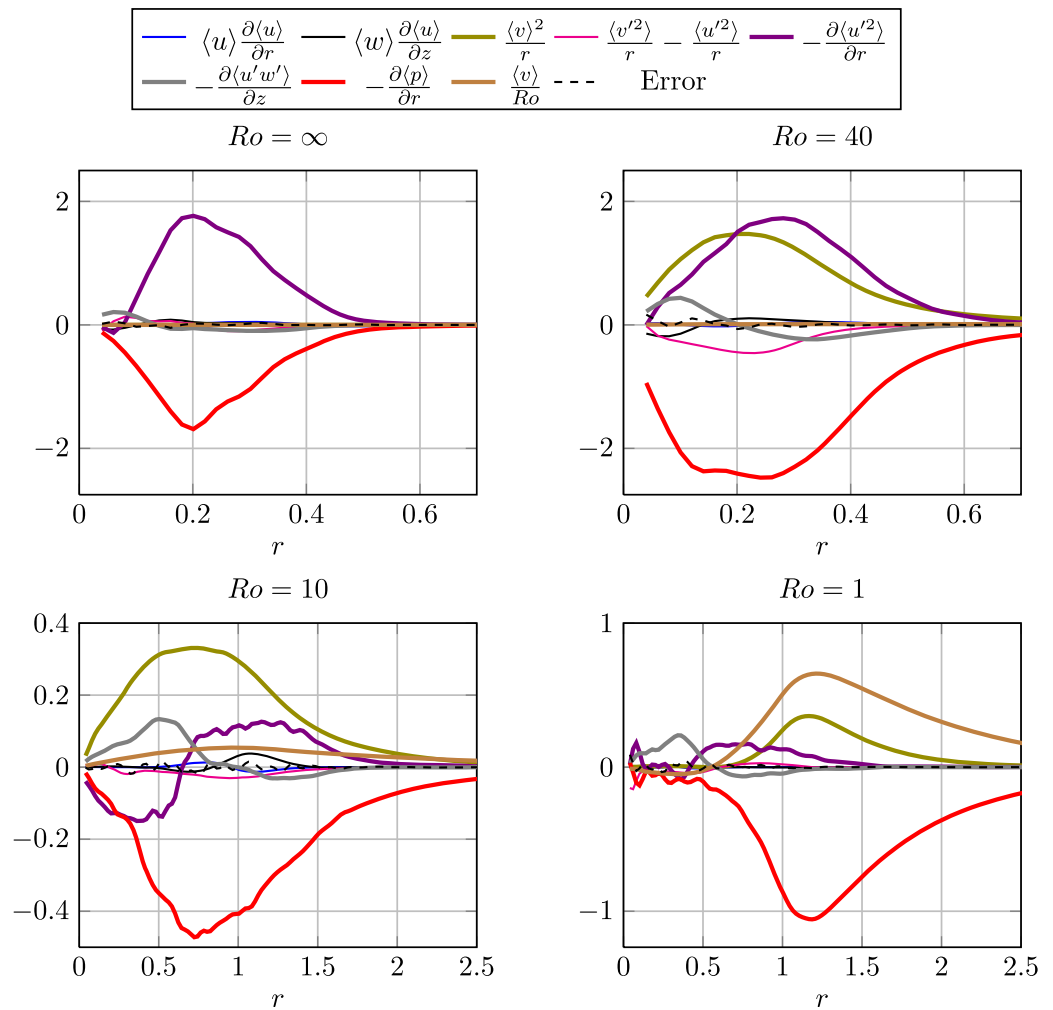


Figure 9. Radial momentum budget at $z = 1.4$ for $Ro = \infty, 40, 10,$ and 1 .

Angular momentum conservation, combined with large entrainment velocities near the plume source, produce significant mean swirl speeds in rotating plumes, and dramatically change radial momentum balances. As shown below, nonnegligible cyclostrophic contributions directly impact the sign of the vertical pressure gradient leading to instabilities under which a rotating plume will develop the mean anticyclonic precession described in section 3.

6.3. Vertical Momentum

Individual contributions to the vertical momentum budget,

$$\langle u \rangle \frac{\partial \langle w \rangle}{\partial r} + \langle w \rangle \frac{\partial \langle w \rangle}{\partial z} = -\frac{\partial \langle p \rangle}{\partial z} + Ri \langle \theta \rangle - \left[\frac{1}{r} \frac{\partial \langle r \langle u'w' \rangle \rangle}{\partial r} + \frac{\partial \langle w'^2 \rangle}{\partial z} \right], \quad (20)$$

are shown in Figure 10. The results for the $Ro = \infty$ plume show that, to first-order, the vertical advection of momentum is balanced by the turbulent transport in the radial direction and the buoyancy. This distribution resembles that found in the heat budget where the vertical advective transport of heat was mostly balanced by the radial turbulent transport and, to a lesser extent, the stratification (see Figure 8).

The balance at $Ro = 40$ shows an increase in the relative importance of the vertical turbulent flux term. The mean vertical advection and radial turbulent flux, along with the buoyancy, still form the dominant balance although their magnitude has decreased with respect to the $Ro = \infty$ case at $z = 1.4$. Importantly, the pressure gradient term, still relatively small, has changed sign in the plume core region. In other words,

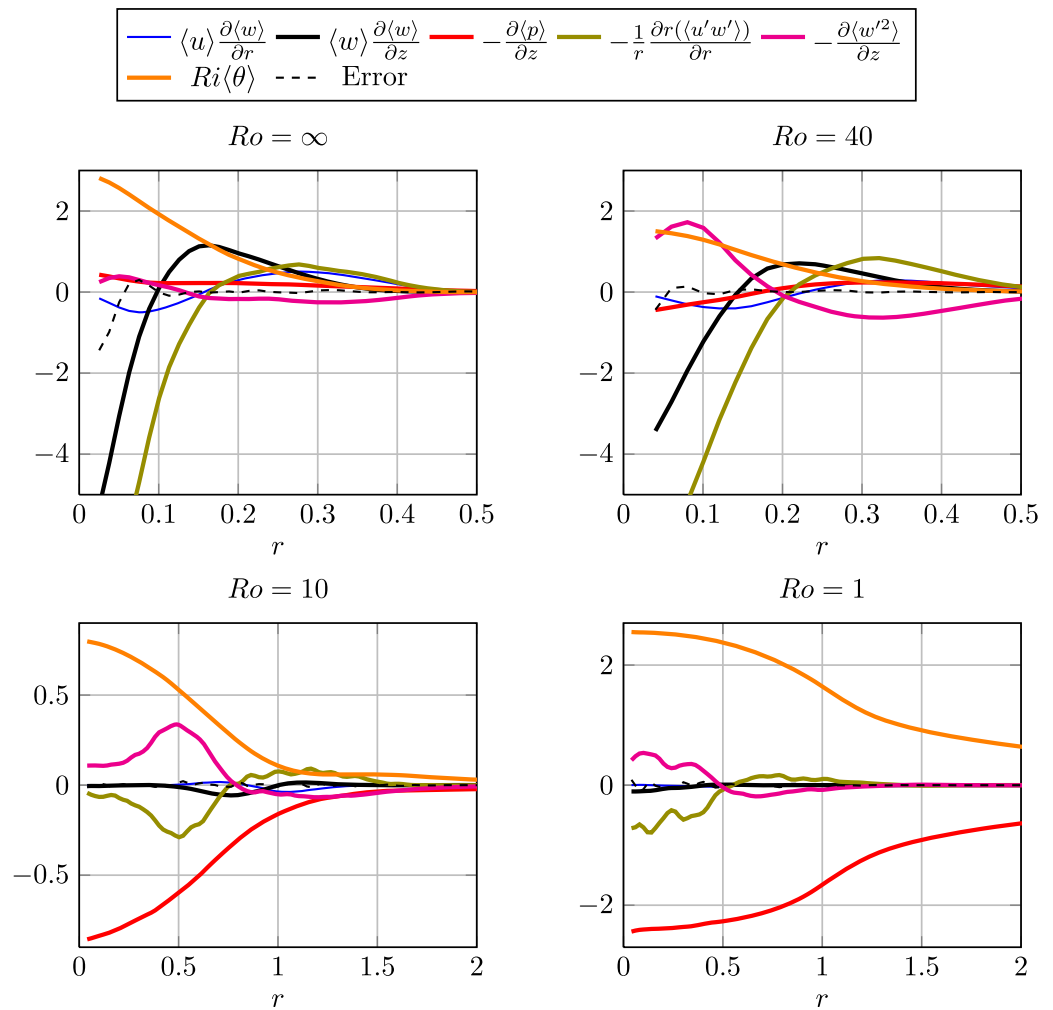


Figure 10. Vertical momentum budget at $z = 1.4$ for $Ro = \infty, 40, 10,$ and 1 .

rotational effects invert the sign of the mean vertical pressure gradient which becomes positive (adverse) near the z axis.

This crucial difference increases as the rotation rate increases. At $Ro = 10$, the picture changes radically in agreement with observations for the heat budget. The smaller values of mean vertical velocity and gradients result in negligible contributions from the mean vertical advection term. Due to the plume axis deflection, the radial and vertical turbulent transport terms exhibit an off-axis peak. Notably, as observed in the radial momentum budget, turbulent transport terms are of opposite sign reducing their net contribution. The resulting budget is dominated by the balance between the mean buoyancy and the mean pressure vertical gradient, essentially unstable hydrostatic equilibrium in the vertical.

In order to explain the rotation induced change in sign of the mean vertical pressure gradient, we integrate the cyclostrophic radial momentum balance,

$$\langle p \rangle(r, z) = \langle p_{cs} \rangle(r, z) = \int_0^r \frac{\langle v \rangle^2(r', z)}{r'} dr' + f(z) \tag{21}$$

where $\langle p_{cs} \rangle$ denotes the cyclostrophic pressure. The mean vertical pressure gradient, can then be estimated as

$$\frac{\partial \langle p \rangle}{\partial z} \approx \frac{\partial \langle p_{cs} \rangle}{\partial z}. \tag{22}$$

The cyclostrophic term $\langle v \rangle^2/r$ and its radial integral, defined as the cyclostrophic pressure in equation (21), are shown in Figures 11a and 11b, respectively. Two isocontours at $\langle w \rangle = 0.15$ (solid) and $\langle \beta \rangle / \beta_0 = 0.1$

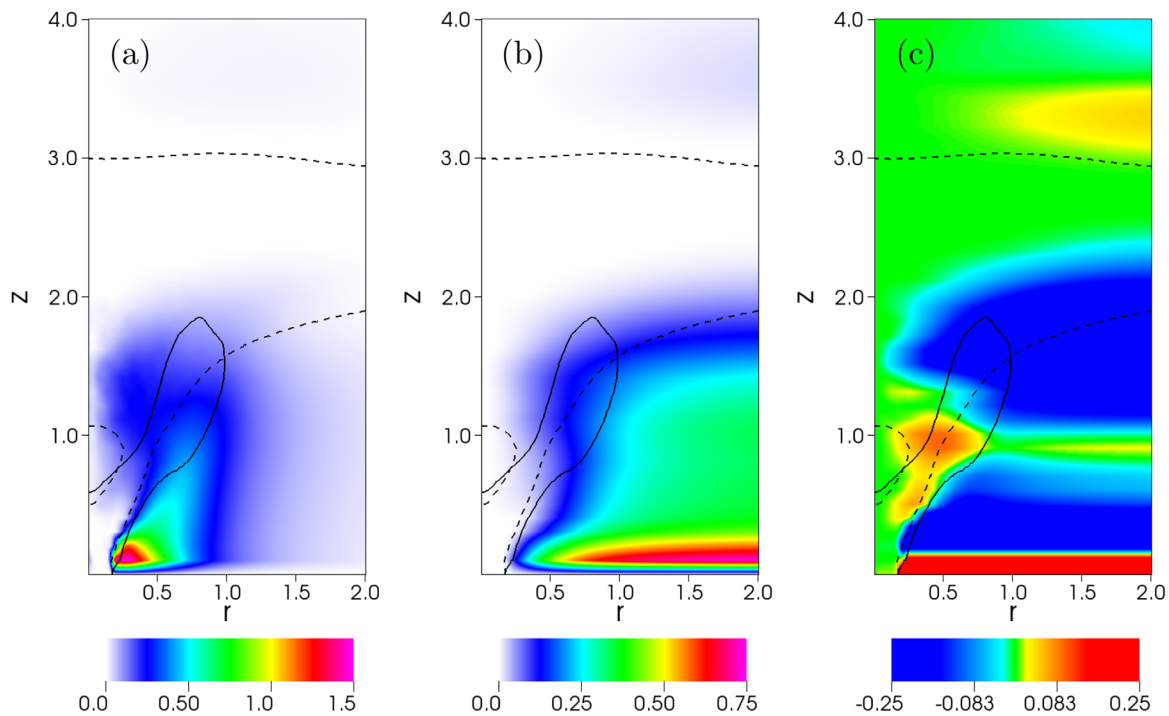


Figure 11. (a) The cyclostrophic term $\frac{\langle v' \rangle^2}{r}$ at $Ro = 10$, (b) the cyclostrophic pressure $\langle p_{cs} \rangle$ as defined in equation (21), and (c) the vertical gradient $\frac{\partial \langle p_{cs} \rangle}{\partial z}$. Solid and dashed contour lines correspond to $\langle w \rangle = 0.15$ and $\langle \beta / \beta_0 \rangle = 0.1$, respectively.

(dashed) are included for plume and lateral intrusion location reference. The vertical gradient, shown in Figure 11c, indicates that the establishment of the cyclostrophic circulation generates a positive pressure gradient along the plume trajectory. This adverse pressure gradient leads to an unstable flow configuration in which the plume is driven off-axis and, by angular momentum conservation, forced to describe an anticyclonic mean precession. In other words, while in a nonrotating plume the vertical momentum induced by the buoyancy is balanced by the vertical advection and the radial turbulent transport term, in the rotating case, the same buoyancy force is opposed by a mean, destabilizing, vertical pressure force. The final flow configuration, as shown in Figure 4, is characterized by a mode one in the azimuthal direction corresponding to the plume-wake pair in continuous anticyclonic precession around the z axis.

The results for $Ro = 1$ show that, as it happens in the radial momentum budget, as rotation increases the turbulent terms are suppressed. The hydrostatic balance between the mean buoyancy and the (positive) vertical pressure gradient discussed for $Ro = 10$ is reinforced with an increase in the magnitude of both contributions.

6.4. Turbulent Kinetic Energy

Rotation, even at moderate Rossby numbers, leads to significant changes in the plume dynamics. These effects also alter dramatically the budget of turbulent kinetic energy $K = \frac{1}{2} \langle u'_i u'_i \rangle$ defined in equation (23) and shown in Figure 12. The symbol ϵ stands here for all the terms not explicitly solved: pressure terms, turbulent transport, molecular viscous transport, and dissipation.

$$\begin{aligned} \langle u \rangle \frac{\partial K}{\partial r} + \langle w \rangle \frac{\partial K}{\partial z} = & \\ - \langle u^2 \rangle \frac{\partial \langle u \rangle}{\partial r} - \langle u' w' \rangle \frac{\partial \langle u \rangle}{\partial z} - \langle u' v' \rangle \frac{\partial \langle v \rangle}{\partial r} - \langle v' w' \rangle \frac{\partial \langle v \rangle}{\partial z} & \quad (23) \\ - \langle u' w' \rangle \frac{\partial \langle w \rangle}{\partial r} - \langle w^2 \rangle \frac{\partial \langle w \rangle}{\partial z} - \frac{\langle u \rangle}{r} \langle v^2 \rangle + Ri \langle w' \theta' \rangle + \epsilon & \end{aligned}$$

In the nonrotating plume, the turbulent kinetic energy is produced mainly by shear stress via the term $\langle u w' \rangle \partial \langle w \rangle / \partial r$ with minor contributions due to the buoyancy and the term $\langle w^2 \rangle \partial \langle w \rangle / \partial z$ resulting in the well-

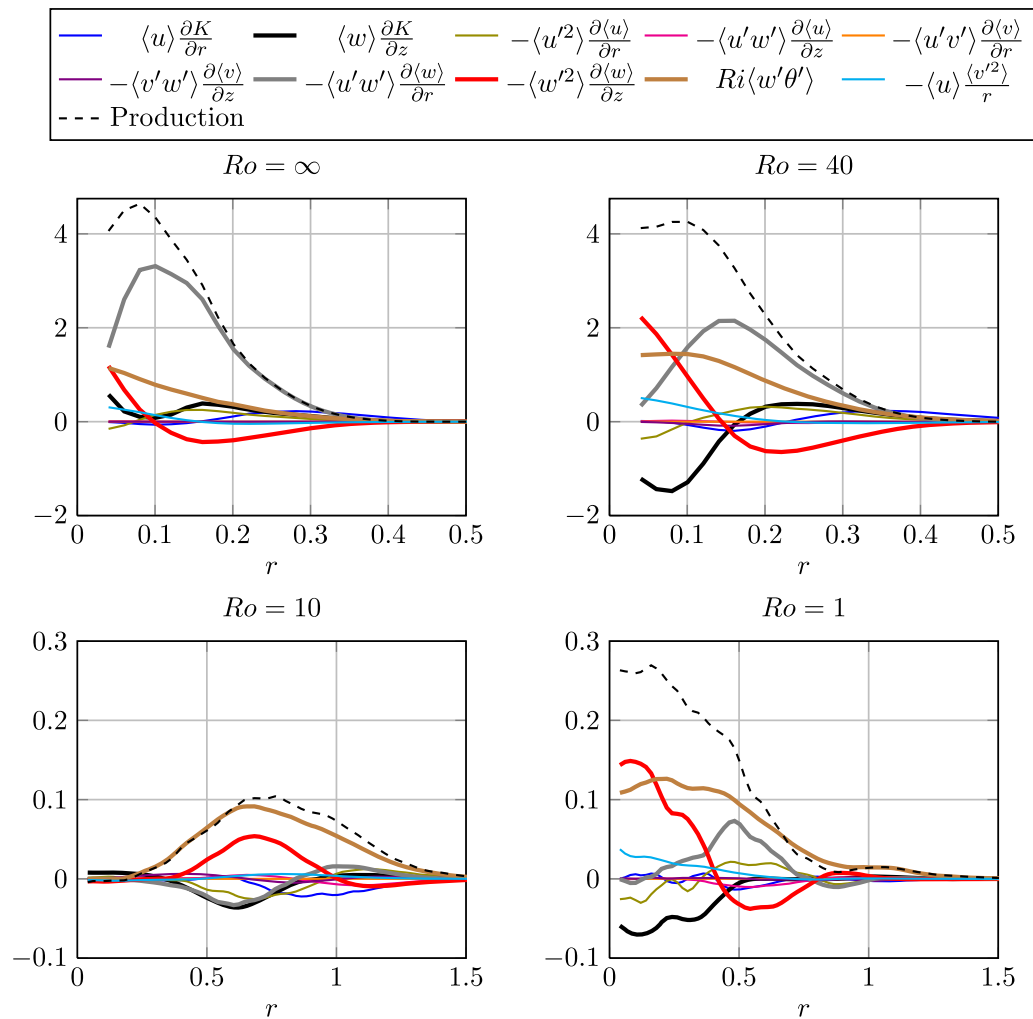


Figure 12. Turbulent kinetic energy budget at $z = 1.4$ for $Ro = \infty, 40, 10,$ and 1 . The total production corresponding to the sum of all the explicit terms in the right hand side of equation (23) is shown as a dashed line.

known “production equals dissipation” balance of thermal plumes in uniform environments [Tennekes and Lumley, 1972].

Contrarily, as the Rossby number decreases and the plume bends reducing the magnitude of the mean radial gradients (see Figure 7), the production of turbulent kinetic energy via mean shear decays to be a relatively minor contribution at $Ro = 10$ and $Ro = 1$. Instead, as rotation speed increases, K becomes mainly produced by the buoyancy contribution. Results also show that while the total K production at $z = 1.4$ (dashed line) for the $Ro = 40$ plume is very similar to that in the nonrotating case, at $Ro = 10$ this quantity decayed by one order of magnitude. Increasing the rotation rate up to $Ro = 1$ leads to a change in this trend and the K production increases with respect to the $Ro = 10$ plume. This is in agreement with the change of regime between $Ro = 10$ and $Ro = 1$ discussed above.

Despite the similar values of turbulent kinetic energy production at $Ro = \infty$ and $Ro = 40$ at $z = 1.4$ shown in Figure 12, the results in Figure 13c reveal that, at that location, the rotating plume has larger values of K than the nonrotating case. This is explained by the largest production of K closer to the source as shown in Figure 13c that presents the results at $z = 0.6$. At that location, both $Ro = \infty$ and $Ro = 40$ exhibit an off-axis peak in K at $r \approx D/2 = 0.15$ where the mean shear layer is found. The larger production of turbulent kinetic energy at $Ro = 40$ suggest that, although too weak to notably deflect the plume at that z level, rotation effects induce an increase in the velocity fluctuation intensities near the source due to the establishment of

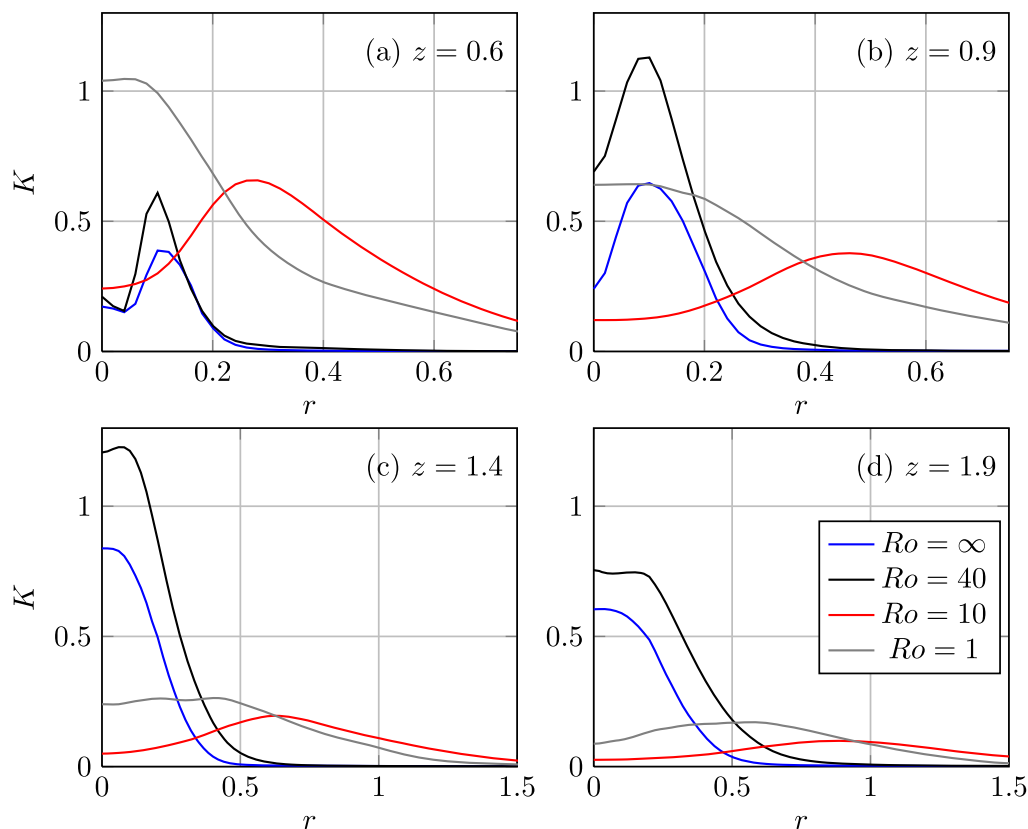


Figure 13. Turbulent kinetic energy at $z=0.6, 0.9, 1.4, 1.9$ for plumes at $Ro = \infty, 40, 10, \text{ and } 1$.

a cyclonic circulation. The vertical advective transport of K explains the larger values of turbulent kinetic energy found downstream at $z = 0.9, 1.4, \text{ and } 1.9$.

In comparison to the plumes at $Ro = \infty$ and $Ro = 40$, the results for the $Ro = 10$ plume show that the peak in K is located further in the radial location as a result of the pronounced plume deflection. Although comparable in magnitude to the two largest values of Rossby at $z = 0.6$, the magnitude of K decays faster and at $z = 1.4$ its maximum value is only around 20% of that at $Ro = 40$. Characterized by a less marked plume axis deflection, the results at $Ro = 1$ reveal that this case has the largest value of turbulent kinetic energy near the source. Again, as in the $Ro = 10$ case, the sustained precession leads to a faster vertical decay in turbulent kinetic energy and at $z = 1.4$ both fastest rotation rate cases exhibit similar values of K .

7. Conclusions

The shape and structure of turbulent buoyant plumes evolving in stably stratified environments are found to be strongly affected by rotation. Results show that as the Rossby number decreases from $Ro = \infty$ to $Ro = 10$ the vertical location of the lateral intrusion decreases and vertical momentum and buoyancy fluxes decay significantly. Overall, rotating plumes are shorter with lower and thicker lateral intrusions. The present numerical results indicate a 25% decrease in the maximum plume height at $Ro = 10$ compared to the nonrotating case.

Dynamically, the primary effect of rotation is the establishment of cyclogeostrophic balance in the near-field radial momentum budget [Speer and Marshall, 1995] and, consequently, the generation of an adverse vertical pressure gradient. Without an inward mass flux, the plume cannot directly and vertically convect as for nonrotating plumes. The result, consistent with experimental observations [Helfrich and Battisti, 1991], is a tilted plume with the axis directed at an angle to the vertical and the establishment of a persistent anticyclonic precession.

The organized, nearly period precession of a tilted plume axis produces three-dimensional, phase-averaged mean fields. As such, rotating plumes share some characteristics with plumes in cross flows. However, unlike a plume in a uniform cross flows, a precessing plumes continuously interacts with its own wake. The present numerical results show clear signals of organized precession in both off-axis time series of vertical velocity and scalar concentration and in Empirical Orthogonal Functions of the vertical velocity field that exhibit mode one azimuthal structure.

In a deepwater oil blowout with a representative Rossby number around $Ro = 10$, estimations of the linear velocity of the precessing plume axis and the typical deep ocean current speed are of the same order. Specifically, using an approximate inlet buoyancy flux for the DWH $B_{DWH} = 0.37 \text{ ms}^4 \text{ s}^{-3}$ and buoyancy frequency $N_{DWH} = 10^{-3} \text{ s}^{-1}$, the velocity and length scales are $U_{DWH} = (B_{DWH} N_{DWH})^{1/4} \approx 0.14 \text{ m s}^{-1}$ and $L_{DWH} = U_{DWH} / N_{DWH} \approx 140 \text{ m}$, respectively. The resulting precession frequency $\tilde{f}_{DWH} = \tilde{f}_p (L_0 / U_0) / (L_{DWH} / U_{DWH}) = 0.15 N_{DWH} = 1.5 \times 10^{-4} \text{ s}^{-1}$ can be used to estimated the precession linear velocity at $\tilde{r}_p = r_p L_{DWH} = 140 \text{ m}$ as $\tilde{u}_p = 2\pi \tilde{r}_p \tilde{f}_{DWH} \approx 13 \text{ cms}^{-1}$. As such, the effects of rotation on pollutant dispersion in deepwater blowouts are potentially relevant even in the presence of a background cross flow.

Rotation at moderate Rossby numbers also significantly impacts the structure and magnitude of plume turbulence. Turbulent kinetic energy budgets indicate marked reduction in the fluctuating kinetic energy and mechanical production from mean shear as rotation increases. At $Ro = 10$, the main source of turbulent kinetic energy is due to buoyancy production. The three-dimensional nature of the tilted plume implies that vertical turbulent transport terms are no longer negligible compared to those in the radial direction further complicating standard turbulence modeling approaches.

In summary, despite the very small spatial scales of the injection, and relatively large buoyancy anomalies associated with the combined oil and gas effluent, planetary rotation emerges as a potentially important factor in the plume evolution. Classical plume models, including those used operationally to diagnose plume development from deep water spills, do not consider rotation and therefore omit above effects. It would be interesting to revisit the DWH plume observations from the perspective provided by the present analysis.

Acknowledgments

This research was made possible by a grant from The Gulf of Mexico Research Initiative. Data are publicly available through the Gulf of Mexico Research Initiative Information & Data Cooperative (GRIIDC). Additional computer resources have also been provided by City University of New York High Performance Computing Center under NSF grants CNS-0855217, CNS-0958379, and ACI-1126113. Data set containing the statistics for the cases presented in this work can be downloaded from: <https://data.gulfresearchinitiative.org/data/R4.x265.250:0003>.

References

- Applequist, E., and P. Schlatter (2014), Simulating the laminar von kármán flow in nek5000, KTH Royal Institute of Technology.
- Devenish, B. J., G. G. Rooney, H. N. Webster, and D. J. Thompson (2010a), The entrainment rate for buoyant plumes in a cross flow, *Boundary Layer Meteorol.*, *134*, 411–439.
- Devenish, B. J., G. G. Rooney, and D. J. Thomson (2010b), Large-eddy simulations of a buoyant plume in uniform and stably stratified environments, *J. Fluid Mech.*, *652*, 75–103.
- Deville, M. O., P. F. Fischer, and E. H. Mund (2002), *High-Order Methods for Incompressible Fluid Flow*, Cambridge Univ. Press, Cambridge, U. K.
- Fabregat, A., W. K. Dewar, T. M. Özgökmen, A. C. Poje, and N. Wieners (2015), Numerical simulations of turbulent thermal, bubble and hybrid plumes, *Ocean Modell.*, *90*, 16–28.
- Fernando, H. J. S., R.-R. Chen, and B. A. Ayotte (1998), Development of a point plume in the presence of background rotation, *Phys. Fluids*, *10*, 2369–2383.
- Fischer, P. F., and J. S. Mullen (2001), Filter-based stabilization of spectral element methods, *C. R. Acad. Sci. – Sér. I*, *332*, 265–270.
- Fischer, P. F., J. W. Lottes, and S. G. Kerkemeier (2008), Nek5000 web page. [Available at <http://nek5000.mcs.anl.gov>.]
- Goodman, J. C., G. C. Collins, J. Marshall, and R. T. Pierrehumbert (2004), Hydrothermal plume dynamics on Europa: Implications for chaos formation, *J. Geophys. Res.*, *109*, E03008, doi:10.1029/2003JE002073.
- Graham, R., W. K. Reilly, F. Beinecke, D. Boesch, T. D. Garcia, C. A. Murray, and F. Ulmer (2011), Deep water: The gulf oil disaster and the future of offshore drilling, Natl. Comm. on the BP Deepwater Horizon Oil Spill and Offshore Drill.
- Helfrich, K. R., and T. M. Battisti (1991), Experiments on baroclinic vortex shedding from hydrothermal plumes, *J. Geophys. Res.*, *96*, 12,511–12,518.
- Jiang, H., and J. A. Breier (2014), Physical controls on mixing and transport within rising submarine hydrothermal plumes: A numerical simulation study, *Deep Sea Res., Part I*, *92*, 41–55.
- Julien, K., S. Legg, J. McWilliams, and J. Werne (1999), Plumes in rotating convection. Part 1. Ensemble statistics and dynamical balances, *J. Fluid Mech.*, *391*, 151–187.
- Karamanos, G.-S., and G. E. Karniadakis (2000), A spectral vanishing viscosity method for large-eddy simulations, *J. Comput. Phys.*, *163*(1), 22–50.
- Koal, K., J. Stiller, and H. Blackburn (2012), Adapting the spectral vanishing viscosity method for large-eddy simulations in cylindrical configurations, *J. Comput. Phys.*, *231*(8), 3389–3405.
- Lavelle, J. W. (1997), Buoyancy-driven plumes in rotating, stratified cross-flows: Plume dependence on rotation, turbulence mixing and cross-flow strength, *J. Geophys. Res.*, *102*, 3405–3420.
- Lehr, B., S. Bristol, and A. Passolo (2010), Oil Budget Calculator Deepwater Horizon, Technical Documentation, A Report to the National Incident Command, November 2010. [Available at http://www.restorethegulf.gov/sites/default/files/documents/pdf/OilBudgetCalc_Full_HQ-Print_111110.pdf.]

- Lubchenco, J., M. K. McNutt, G. Dreyfus, S. A. Murawski, D. M. Kennedy, A. P. T., S. Chu, and T. Hunter (2012), Science in support of the deep-water horizon response, *Proc. Natl. Acad. Sci. U. S. A.*, *109*, 20,121–10,221.
- Marqués, F., and J. M. López (2014), Spontaneous generation of a swirling plume in a stratified ambient, *J. Fluid Mech.*, *761*, 443–463.
- Maxworthy, T., and S. Narimousa (1994), Unsteady, turbulent convection into a homogeneous, rotating fluid, with oceanographic applications, *J. Phys. Oceanogr.*, *24*, 865–887.
- McNutt, M. K., R. Camilli, T. J. Crone, G. D. Guthrie, P. A. Hsieh, T. B. Ryerson, O. Savas, and F. Shaffer (2012), Review of flow rate estimates of the deepwater horizon oil spill, *Proc. Natl. Acad. Sci. U. S. A.*, *109*, 20,260–20,267.
- Morton, B. R., G. Taylor, and J. S. Turner (1956), Turbulent gravitational convection from maintained and instantaneous sources, *Proc. R. Soc. London Ser. A*, *24*, 1–23.
- Özgökmen, T. M., T. Iliescu, and P. F. Fischer (2009a), Large eddy simulation of stratified mixing in a three-dimensional lock-exchange system, *Ocean Modell.*, *26*(34), 134–155.
- Özgökmen, T. M., T. Iliescu, and P. F. Fischer (2009b), Reynolds number dependence of mixing in a lock-exchange system from direct numerical and large eddy simulations, *Ocean Modell.*, *30*(23), 190–206.
- Pham, M. V., F. Plourde, and S. D. Kim (2006), Large-eddy simulation of a pure thermal plume under rotating conditions, *Phys. Fluids*, *18*, 015,101–1–015,101–15.
- Pham, M. V., F. Plourde, and S. Doan-Kim (2007), Direct and large-eddy simulations of a pure thermal plume, *Phys. Fluids*, *19*, 125,103.
- Pham, M. V., F. Plourde, and S. D. Kim (2011), Unstable process identification in a pure thermal plume under forced rotating conditions, *Exp. Heat Transfer*, *24*, 151–167.
- Plourde, F., M. V. Pham, S. Doan-Kim, and S. Balachandar (2008), Direct numerical simulation of a rapidly expanding thermal plume: Structure and entrainment interaction, *J. Fluid Mech.*, *604*, 99–123.
- Plume Calculation Team (2010), Deepwater horizon release estimate of rate by PIV, Report to U.S. Dep. of Int. [Available at <https://www.doi.gov/deepwaterhorizon/loader.cfm?csModule=security/getfile&PageID=68011>.]
- Richards, T. S., Q. Aubourg, and B. R. Sutherland (2014), Radial intrusions from turbulent plumes in uniform stratification, *Phys. Fluids*, *26*, 036,602–1–036,602–17.
- Riedinger, X., P. Meunier, and S. Le Dizès (2010), Instability of a vertical columnar vortex in a stratified fluid, *Exp. Fluids*, *49*, 673–681.
- Shabbir, A., and W. K. George (1994), Experiments on a round turbulent buoyant plume, *J. Fluid Mech.*, *275*, 1–32.
- Sheremet, V. A. (2004), Laboratory experiments with tilted convective plumes on a centrifuge: A finite angle between the buoyancy force and the axis of rotation, *J. Fluid Mech.*, *506*, 217–244.
- Socolofsky, S. A., and E. E. Adams (2005), Role of slip velocity in the behavior of stratified multiphase plumes, *J. Hydraul. Eng.*, *131*, 273–282.
- Speer, K. G., and J. Marshall (1995), The growth of convective plumes at seafloor hot springs, *J. Mar. Res.*, *53*, 1025–1057.
- Tennekes, H., and J. Lumley (1972), *A First Course in Turbulence*, MIT Press, Cambridge, Mass.